A robust fractional-order sliding mode control technique for piezoelectric nanopositioning stages in trajectory-tracking applications

Rui Xu [a,b], Zhongshi Wang [a], Miaolei Zhou [c], Dapeng Tian [a,b,*]

[a] *Key Laboratory of Airborne Optical Imaging and Measurement, Changchun Institute of Optics, Fine Mechanics and Physics, Chinese Academy of Sciences, Changchun 130033, China*
[b] *University of Chinese Academy of Sciences, Beijing 100049, China*
[c] *College of Communication Engineering, Jilin University, Changchun 130012, China*

ARTICLE INFO

ABSTRACT

High-precision control of the piezoelectric nanopositioning stages is becoming a key technique in some precision manufacturing equipment. However, the piezoelectric nanopositioning stages suffer from the hysteresis effect and load disturbance, which damage its positioning accuracy. This paper proposes a fractional-order sliding mode tracking control method combining the fractional-order sliding mode surface and a new two-power reaching law to achieve high-precision tracking control of the piezoelectric nanopositioning stages under different loads. The fractional-order sliding mode surface effectively alleviates its chattering problem. The new two-power reaching law improves the convergence rate of the proposed controller. We conduct a rigorous theoretical analysis of the convergence interval and stability of the proposed controller. To evaluate the performance of the proposed controller, we carry out comparative trajectory tracking experiments on the piezoelectric nanopositioning stages. Results show that the proposed controller exhibits a satisfactory tracking performance even under different loads. Moreover, comparisons show that the proposed fractional-order sliding mode tracking controller outperforms the conventional PID and sliding mode control methods. The tracking performance of the proposed fractional-order sliding mode control method is improved by 59.17% and 39.42% compared with the PID and sliding mode control methods when tracking a sinusoidal signal with a frequency of 100 Hz.

1. Introduction

High-precision positioning control of the piezoelectric nanopositioning stages (PNS) has been attracting increasing attention from researchers, owing to its widespread applications, including the atomic force microscope [1,2], precision mirror alignment [3], and micromanipulation [4]. However, the hysteresis of the piezoceramic material severely damages the positioning accuracy of the micro-nano platform. As shown in Fig. 1, hysteresis curves vary with the frequency of the input signal. Thus, a suitable control strategy is imperative to achieve high-precision tracking positioning of the PNS under different loads.

Recently, several types of control methods have been proposed [5–7], to deal with the hysteresis behavior of the PNS. The hysteresis effect is effectively eliminated by implementing the exact inverse hysteresis model as the feed-forward compensator, such as the inverse Bouc–Wen model [8], inverse Duhem model [9], and Prandtl–Ishlinskii model [10] (including Play or Stop operators), etc. Li et al. adopted an inverse multiplicative structure to construct several feed-forward compensators,

where the adopted hysteresis models include the Duhem, Preisach, and Krasnosel'skii–Pokrovskii models, among others [11,12]. Considering that the residual error includes modeling uncertainties and external disturbances of the platform, the closed-loop control method combined with the feed-forward compensator is designed as a hybrid controller, where the most commonly adopted closed-loop control method includes the PID control [13], sliding mode control (SMC) [14], and iterative learning control [15], etc. Tan et al. proposed an adaptive conditional servo compensator without requiring explicit inversion of the hysteresis to achieve nanopositioning tracking control of stages driven by piezoelectric materials [16]. However, the performance of the compensator is heavily dependent on the modeling accuracy of the inverse hysteresis model. Therefore, several inversion-free control methods were studied in the field of micro-nano positioning control based on piezoelectric actuators [17,18]. Xu et al. proposed a self-adaptive compensation control method without an inverse hysteresis model to
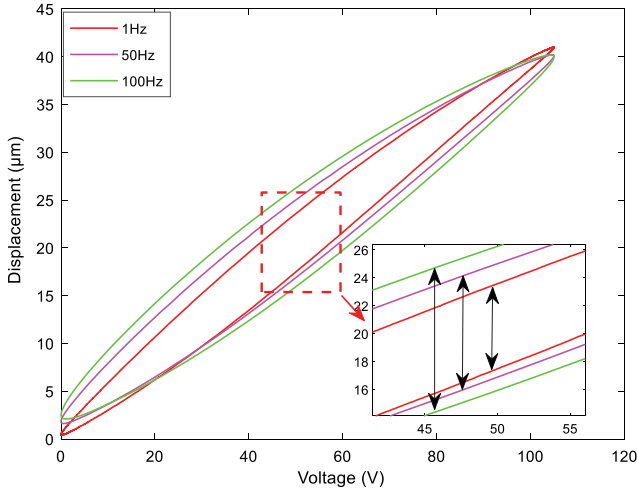
Fig. 1. Hysteresis characteristics of the PNS.

Fig. 2. Electrical model of the PNS.

eliminate the hysteresis behavior of the PNS [19]. An inversion-free predictive controller, based on the dynamic linearized neural network model, was designed for the piezoelectric actuators [20]. Further, other control strategies have been studied in [21,22] and likewise yielded excellent performances.

In particular, a robust SMC technique emerged as an attractive control strategy in the nanopositioning field, owing to its inherent merits of highly robust performance to external disturbance or parameter uncertainty, fast response, and better transient performance [23,24]. The purpose of the SMC is to force the system state trajectory onto a defined sliding mode surface, and to maintain it on the surface for the subsequent time. However, it is difficult to design an appropriate sliding mode surface to guarantee its convergence. To address this issue, the fractional-order calculation was introduced into the design of the sliding mode surface. The extra degrees of freedom from the fractional-order sliding mode surface (FOSMS) improve the performance of the corresponding controller in comparison with the integer-order sliding mode controller [25,26]. The fractional-order sliding mode controller was applied predominantly in servo drive control (such as permanent magnet synchronous motors [27,28] and power electronic buck converters [29]) owing to its high performance.

From a practical perspective, the system states of the traditional SMC method do not remain on the FOSMS due to the discontinuous control action derived from the modeling uncertainties and exterior disturbances. Consequently, the traditional SMC usually generates the chattering phenomenon, which may give rise to the undesired high-frequency dynamic oscillation and even deteriorate the tracking or positioning accuracy of the PNS. To tackle the inherent chattering problem of the traditional SMC method, a notable effort has been studied by numerous scholars, and several methods were proposed in the literature. For example, Xu et al. utilized an uncertainty and disturbance estimator to realize a chattering-free sliding mode controller for the high-precision tracking control of piezo-driven stages [30]. Further, the boundary layer technique [31], high-order sliding mode control method [32,33], adaptive SMC strategy [34], and low-pass filtering based SMC scheme [35] were introduced to alleviate the chattering effect.

This study is mainly bank for the current problems in the design of the SMC method. It also proposes a FOSMC method with a new two-power reaching law to implement high accuracy control of the PNS. The proposed two-power reaching law is highly efficient for addressing modeling uncertainty and load disturbance of the PNS. The chattering issue is effectively alleviated by the FOSMS. The stability and convergence region of the presented FOSMC technique are analyzed in
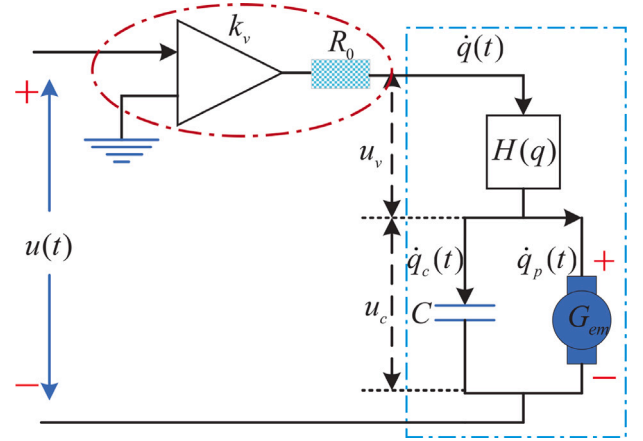
detail and demonstrated using the finite-time and Lyapunov theories. Finally, some comparative experiments are carried out on the PNS to verify the superiority of proposed FOSMC technique.

The remainder of this paper is organized as follows. System modeling and problem formulation are described in Section 2. Then, a FOSMC approach is designed to achieve tracking control of the PNS, and the convergence and stability of the proposed controller are analyzed in Section 3. Section 4 describes the experimental setup and the identified parameters of the Duhem model. This forms the basis for the tracking experiments of the PNS. Some comparative tracking experiments are carried out to verify the performance of the proposed FOSMC method in Section 5. Section 6 presents the conclusion and future prospects.

2. System modeling and problem formulation

The modeling of the PNS requires consideration of piezoelectric ceramic circuits, drive amplifier circuits, and flexible hinge structures. As shown in Fig. 2, it is the circuit model of the PNS. The driver amplifier is described as a series circuit of the gain k_v and the resistance R_0, the piezoelectric ceramic actuator is described as a series–parallel circuit of capacitors C and electromechanical converters G_{em}. C is the total capacitance of piezoelectric ceramics, q is the total charge of the piezoelectric ceramics actuator, q_c and q_p are the charge stored in the capacitor C and induced charge from piezoelectric effect. Next, we define $u_a(t)$ as the voltage from the piezoelectric effect, which is equal to the voltage $u_c(t)$ of the capacitor C. So, we can obtain the circuit equation as

$$\begin{cases} R_0\dot{q}(t) + u_v(t) + u_c(t) = k_v u(t) \\ q_p(t) = G_{em}x(t) \\ u_c(t) = q_c(t)/C \\ q(t) = q_c(t) + q_p(t) \\ u_v(t) = H(q), \end{cases} \tag{1}$$

where $u(t)$ is the input voltage of the PNS, $x(t)$ is the output displacement. The formula (1) is rewritten as

$$R_0C\dot{q}(t) + q(t) - G_{em}x(t) = Ck_v[u(t) - \frac{1}{k_v}H(q)]. \tag{2}$$

Next, the mechanical characteristics of the flexible hinge structure is modeled as

$$m\ddot{x}(t) + b\dot{x}(t) + kx(t) = G_{em}u_a(t), \tag{3}$$

where m, b, and k are the equivalent mass, damping, and stiffness, respectively.

Combining (2) with (3), it can be obtained that

$$\dddot{x}(t) + (\frac{1}{R_0 C} + \frac{b}{m})\ddot{x}(t) + (\frac{b}{mR_0 C} + \frac{kC + G_{em}^2}{mC})\dot{x}(t) \\ + \frac{k}{mR_0 C}x(t) = \frac{k_v G_{em}}{mR_0 C}(u(t) - \frac{1}{k_v}H(q)). \quad (4)$$

According to (4), the PNS is described as a third-order system. In this work, limited by the operating characteristics of the PNS, we do not consider the high frequency characteristics of this stage, established model (4) is reduced to the following Duhem model form:

$$\begin{cases} \dot{x}(t) = a_0 x(t) + a_1 u(t) + a_2 \hbar(t) + \phi(t) \\ \dot{\hbar}(t) = \alpha |\dot{u}(t)| [f(u(t)) - \hbar(t)] + \dot{u}(t) g(u(t)) \\ y(t) = x(t), \end{cases} \quad (5)$$

Herein, $y(t)$ is the output of the model; $\hbar(t)$ is the duhem operator, which represents the hysteresis part $H(q)$ of the piezoelectric ceramic. $f(\cdot)$ and $g(\cdot)$ are piecewise continuous functions, which are used to approach the hysteresis part of the Duhem model; $\dot{x}(t)$, $\dot{u}(t)$, and $\dot{\hbar}(t)$ are the first order time derivatives of $x(t)$, $u(t)$, and $\hbar(t)$ with respect to time, respectively; $a_0 = -k/(b + kCR_0 + G_{em}^2 R_0)$, $a_1 = -(k_v G_{em})/(b + kCR_0 + G_{em}^2 R_0)$, $a_2 = -G_{em}/(b + kCR_0 + G_{em}^2 R_0)$ represent the stage systems parameters; $\phi(t)$ denotes the system perturbation produced by uncertain parameters and external disturbance.

Followingly, the unknown functions $f(\cdot)$ and $g(\cdot)$ are obtained by the Weierstrass approximation theorem. This method has the advantages of strong approximation ability and a low computational complexity. In this study, $f(\cdot)$ and $g(\cdot)$ are replaced by two polynomial functions $\hat{f}(\cdot)$ and $\hat{g}(\cdot)$, respectively, which are expressed as:

$$\begin{cases} \hat{f}(u(t)) \cong f_0 + f_1 u(t) + \cdots f_{\varrho_1} u^{\varrho_1}(t) = \sum_{i=0}^{\varrho_1} f_i u^i(t) \\ \hat{g}(u(t)) \cong g_0 + g_1 u(t) + \cdots g_{\varrho_2} u^{\varrho_2}(t) = \sum_{j=0}^{\varrho_2} g_j u^j(t), \end{cases} \quad (6)$$

where f_i and g_i are the constants, ϱ_1 and ϱ_2 are the orders of the $\hat{f}(\cdot)$ and $\hat{g}(\cdot)$, respectively. Thus, the Duhem hysteresis model is reformulated as:

$$\begin{cases} \dot{x}(t) = a_0 x(t) + a_1 u(t) + a_2 \hat{\hbar}(t) + \phi(t) \\ \dot{\hat{\hbar}}(t) = \alpha |\dot{u}(t)| (\hat{f}(u(t)) - \hat{\hbar}(t)) + \dot{u}(t) \hat{g}(u(t)) \\ y(t) = x(t). \end{cases} \quad (7)$$

where $\hat{h}$ is the estimated value of $\hbar$ based on $\hat{f}(\cdot)$ and $\hat{g}(\cdot)$.

The objective of this study is to achieve a superior positioning performance of the PNS with the lump disturbance $\phi(t)$. To suppress the tracking error and achieve a desired locating ability, a novel control technique is devised in the following section.

3. Fractional-order sliding mode controller

A FOSMC strategy is proposed to eliminate the hysteresis and suppress the perturbation caused by parameter uncertainties and unknown disturbances (such as the external loads) of the PNS. We introduce the fractional calculus into the design of the proposed FOSMC method, it exhibits low chattering in the sliding motion. A new reaching law forces the system states to reach the sliding manifold in finite time, and improves convergence rate of system states. These improve the performance of the FOSMC and achieve high precision tracking control of the PNS.

3.1. Fractional-order sliding mode surface

At first, we design a FOSMS, written as:

$$\sigma(t) = \bar{e}(t) + \lambda(_0 D_t^r \bar{e}(t)), \quad (8)$$

where $\bar{e}(t)$ is the error between the desired output state $x_d(t)$ and the actual output state $x(t)$ of the PNS; λ is a constant, which influences the reaching rate of the system states. $_0 D_t^r(\cdot)$ is the fractional calculus,

and r is a constant and it satisfies $0 < r < 1$. Generally, the fractional calculus $_0 D_t^r(\cdot)$ is described as:

$$_0 D_t^r(\cdot) = \begin{cases} \frac{d^r}{dt^r} & R(r) > 0 \\ 1 & R(r) = 0 \\ \int_0^t (d\tau)^{-r} & R(r) < 0, \end{cases} \quad (9)$$

where $R(r)$ represents the real part of r. There are several definitions for the fractional calculus in the existing literature [36,37]. Riemann–Liouville fractional calculus is an important and commonly definition, which is expressed as follows [38]:

$$_{t_0}^{RL} D_t^r f(t) = \frac{1}{\Gamma(\varsigma - r)}(\frac{d}{dt})^\varsigma \int_{t_0}^t \frac{f(\tau)}{(t-\tau)^{1+r-\varsigma}}, \quad (10)$$

where $\varsigma - 1 < r < \varsigma$, and $\varsigma \in N$. The $\Gamma(\cdot)$ is the Gamma function. In this study, to apply the fractional calculus into the controller, we transform it into Laplace form, and it is given by

$$L(_{t_0}^{RL} D_t^r f(t)) = \int_{t_0}^\infty e^{-st} {}_{t_0} D_t^r f(t) dt \\ = s^r F(s) - \sum_{k=0}^{m-1} s^k {}_{t_0} D_t^{r-k-1} f(t)|_{t=0}, \quad (11)$$

where s is the Laplacian operation; when the initial condition of the $f(t)$ is zero, formula (11) is rewritten as:

$$L(_0^{RL} D_t^r f(t)) = \int_0^\infty e^{-st} {}_0 D_t^r f(t) dt = s^r F(s). \quad (12)$$

In general, the fractional order calculus is difficult to implement directly in engineering. Oustaloup method, as an efficient filter, is widely used to approximate the fractional order calculus because of its advantages of simple calculation and easy engineering implementation. In this study, we use the Oustaloup method to approximate the fractional order calculus, and s^r can be written as:

$$O(s) = (\frac{\sqrt{\omega_L \omega_H}}{\omega_H})^r \prod_{k=-N}^N \frac{1 + s/\omega_k'}{1 + s/\omega_k}, \quad (13)$$

where N is a constant, and $2N + 1$ represents the number of zeros or poles of the function $O(s)$. ω_L and ω_H denote the lower and upper frequencies of the fitting curve, respectively. ω_k and ω_k' are calculated as

$$\omega_k = \omega_L (\frac{\omega_H}{\omega_L})^{\frac{K+N+\frac{1}{2}+\frac{r}{2}}{2N+1}}, \quad (14)$$

$$\omega_k' = \omega_L (\frac{\omega_H}{\omega_L})^{\frac{K+N+\frac{1}{2}-\frac{r}{2}}{2N+1}} \quad (15)$$

In this study, ω_L and ω_H are selected as 1 and 1000, respectively. N is chosen as 1 to balance the computational complexity and approximate precision. For a more detailed discussion of parameters selection for the Oustaloup method, please refer to [39].

We introduce fractional order calculus into the design of sliding mode controller, and the FOSMS is designed. When the sliding mode controller generates sliding mode motion, the states of the FOSMS converge to balance point fast and stably. To illustrate the stability of the proposed FOSMS (the condition for the existence of sliding mode is satisfied), the following lemma is introduced.

Lemma 1 ([40]). *For the fractional-order system:*

$$_0 D_t^r x(t) = A x(t), x(0) = x_0, \quad (16)$$

where r is the differential order, $x \in R^n$ and $A \in R^{n \times n}$, is asymptotically stable if $|arg(eig(A))| > \frac{r\pi}{2}$.

Letting $\sigma = 0$, we obtain

$$_0 D_t^r \bar{e}(t) = -\frac{1}{\lambda}\bar{e}(t). \quad (17)$$
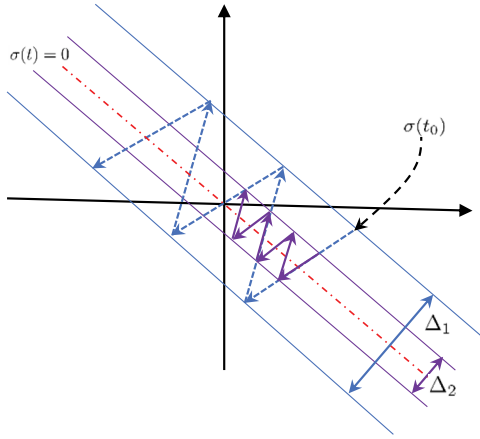
Fig. 3. Converging process comparison between FOSMS and integer order sliding mode surface.

Based on Lemma 1, if $\left|\arg(\mathrm{eig}(-\frac{1}{\lambda}))\right| = \pi > \frac{r\pi}{2}$ is satisfied, the fractional-order system (16) is stable. Because $0 < r < 1$, $0 < \frac{r\pi}{2} < \frac{\pi}{2}$, the $|\arg(\mathrm{eig}(A))| > \frac{r\pi}{2}$ holds always true. Therefore, the FOSMS is asymptotically stable.

Remark 1. The chattering problem of the SMC is caused by the delay of the actual system. As shown in Fig. 3, it notes that the integer-order sliding mode surface converges to the equilibrium point in an exponential law. However, the convergence rate of the FOSMS can be adjusted by the fractional order derivative r. The convergence rate of the FOSMS is less than the convergence rate of the integer-order sliding mode surface by selecting r. The integer-order sliding mode system states are switched in region Δ_1, and the fractional-order sliding mode system states are switched in region Δ_2, and they satisfy $\Delta_1 > \Delta_2$. Therefore, the FOSMS transfers energy more slowly than the integer-order. The FOSMS can effectively reduce the chattering.

3.2. Controller design

Before the design of the FOSMC method, the following assumption and Lemma are introduced.

Assumption 1. The lump disturbance of the PNS is bound and satisfies that $|\phi| \leq \Phi$, where Φ is a positive constant.

Lemma 2 ([41]). *If a continuous, positive definite function $F(t)$ satisfies*

$$\dot{F}(t) \leq \zeta F^{\gamma}(t), \forall t \leq t_0, F(t_0) \geq 0, \tag{18}$$

where two constants ζ and γ satisfy $\zeta > 0$, $0 < \gamma < 1$, then the function $F(t)$ is convergent in finite time.

Theorem 1. *Considering the PNS system is described by (7) with the FOSMS (8), if the control law is (19), the FOSMS $\sigma(t)$ will converge to Ψ.*

$$u(t) = \frac{1}{a_1}[u_1(t) + u_2(t)], \tag{19}$$

with

$$u_1(t) = \dot{x}_d(t) - a_0 x(t) - a_2 \hat{h}(t) + \lambda({}_0 D_t^{r+1} e(t)). \tag{20}$$

$$u_2(t) = k_1 \mathrm{Fal}\left(\sigma(t), \varepsilon_1, \delta_{\Delta_1}\right) + k_2 \mathrm{Fal}\left(\sigma(t), \varepsilon_2, \delta_{\Delta_2}\right). \tag{21}$$

where k_1 and k_2 are positive constants; ε_1 and ε_2 are the parameters of the two-power reaching law, and they satisfy $\varepsilon_1 > 1$, $0 < \varepsilon_2 < 1$, and the function $\mathrm{Fal}\left(\sigma(t), \varepsilon, \delta_{\Delta}\right)$ is described as follows:

$$\mathrm{Fal}\left(\sigma(t), \varepsilon, \delta_{\Delta}\right) = \begin{cases} |\sigma(t)|^{\varepsilon} \mathrm{sgn}(\sigma(t)) & |\sigma(t)| > \delta_{\Delta} \\ \frac{\sigma(t)}{\delta_{\Delta}^{(1-\varepsilon)}} & |\sigma(t)| \leq \delta_{\Delta}, \end{cases} \tag{22}$$

where $\delta_{\Delta} > 0$ is the boundary layer of the Fal function. It is worth noting that the main role of $u_1(t)$ is to make the system states converge to the FOSMS, and the $u_2(t)$ is used to compensate the lump disturbance and keeps the system states on the FOSMS.

Proof. First, we define the Lyapunov function as follows:

$$V(t) = \frac{1}{2}\sigma^2(t). \tag{23}$$

Taking the first-order time derivative of (23),

$$\dot{V}(t) = \sigma(t)\dot{\sigma}(t). \tag{24}$$

Then, taking the first order time derivative of the FOSMS (8),

$$\dot{\sigma}(t) = \ddot{e}(t) + \lambda({}_0 D_t^{r+1} \bar{e}(t)). \tag{25}$$

In view of the first formula in (7), the following formula is shown as:

$$\dot{\sigma}(t) = \dot{x}_d(t) - a_0 x(t) - a_1 u(t) - a_2 \hat{h}(t) - \phi(t) \\ + \lambda({}_0 D_t^{r+1} \bar{e}(t)). \tag{26}$$

Substituting (19) and (26) into (24), leads to

$$\begin{aligned} \dot{V}(t) &= \sigma(t)\left(\dot{x}_d(t) - a_0 x(t) - a_1(u_1(t) + u_2(t))\right. \\ &\quad \left. - a_2 \hat{h}(t) - \phi(t) + \lambda({}_0 D_t^{r+1} \bar{e}(t))\right) \\ &= \left[-k_1 \mathrm{Fal}\left(\sigma(t), \varepsilon_1, \delta_{\Delta_1}\right)\right. \\ &\quad \left. -k_2 \mathrm{Fal}\left(\sigma(t), \varepsilon_2, \delta_{\Delta_2}\right)\right]\sigma(t) - \phi(t)\sigma(t) \\ &\leq \left[-k_1 \mathrm{Fal}\left(\sigma(t), \varepsilon_1, \delta_{\Delta_1}\right)\right. \\ &\quad \left. -k_2 \mathrm{Fal}\left(\sigma(t), \varepsilon_2, \delta_{\Delta_2}\right)\right]|\sigma(t)| + \Phi|\sigma(t)|. \end{aligned} \tag{27}$$

Case 1: when the system state is remote from the FOSMS, i.e., in the distance reaching phase. At this moment, the term $k_1 \mathrm{Fal}\left(\sigma(t), \varepsilon_1, \delta_{\Delta_1}\right)$ plays a key role due to $\varepsilon_1 > 1$. As show in Fig. 4(a), t_1 represents the this distance reaching phase, it shows that the reaching law makes the states approach the FOSMS rapidly.

If $|\sigma(t)| > \delta_{\Delta}$, formula (28) is based on (22) and (27).

$$\begin{aligned} \dot{V}(t) &\leq |\sigma(t)|\left[-k_1 |\sigma(t)|^{\varepsilon_1} \mathrm{sgn}(\sigma(t))\right. \\ &\quad \left. - k_2 |\sigma(t)|^{\varepsilon_2} \mathrm{sgn}(\sigma(t)) + \Phi\right], \end{aligned} \tag{28}$$

and rewritten as follow:

$$\dot{V}(t) \leq -k_2 |\sigma(t)|^{\varepsilon_2+1} - \left(k_1 |\sigma(t)|^{\varepsilon_1} - \Phi\right)|\sigma(t)|. \tag{29}$$

When $k_1 |\sigma(t)|^{\varepsilon_1} - \Phi \geq 0$, in view of (29), it can be obtained that

$$\dot{V}(t) \leq -k_2 |\sigma(t)|^{\varepsilon_2+1} \tag{30}$$

On the basis of the formula (30), there is:

$$\dot{V}(t) \leq -2^{(\varepsilon_2+1)/2} k_2 V^{(\varepsilon_2+1)/2}(t). \tag{31}$$

According to Lemma 2, when the convergence region of the FOSMS is as follows:

$$|\sigma(t)| \leq \left(\frac{\Phi}{k_1}\right)^{\varepsilon_1^{-1}} \tag{32}$$

the control system state converges to a neighborhood of the origin in finite time.

If $|\sigma(t)| \leq \delta_{\Delta}$, the formula (33) according to (22) is

$$\dot{V}(t) \leq \left[-k_1 \delta_{\Delta_1}^{(\varepsilon_1-1)}\sigma(t) - k_2 \delta_{\Delta_2}^{(\varepsilon_2-1)}\sigma(t)\right]|\sigma(t)|$$
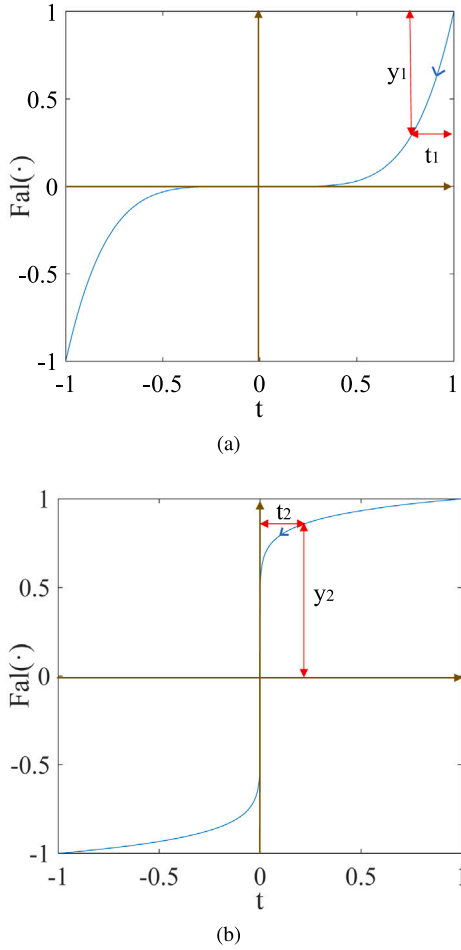
(a)

(b)

Fig. 4. Reaching law function Fal(·) analysis. (a) the distant reaching phase, (b) the close approximation phase.

$$+ \, \Phi \, |\sigma(t)| , \tag{33}$$

and rewritten as follows:

$$\dot{V}(t) \leq -k_2 \delta_{\Delta_2}^{(\varepsilon_2 - 1)} \sigma^2(t) - \left(k_1 \delta_{\Delta_1}^{(\varepsilon_1 - 1)} \sigma(t) - \Phi \right) |\sigma(t)| . \tag{34}$$

When $k_1 \delta_{\Delta_1}^{(\varepsilon_1 - 1)} \sigma(t) - \Phi \geq 0$, based on the formula (34), we have

$$\dot{V}(t) \leq -2 \delta_{\Delta_2}^{(\varepsilon_2 - 1)} k_2 V(t) . \tag{35}$$

According to Lemma 2, To ensure that the FOSMS is convergent in finite time, the convergence region is calculated as:

$$|\sigma(t)| \leq \frac{\Phi}{k_1 \delta_{\Delta_1}^{(\varepsilon_1 - 1)}} . \tag{36}$$

The convergence region of the FOSMS in the distant reaching phase is as follows:

$$\Omega_1 : \left\{ |\sigma(t)| \, | \, |\sigma(t)| \leq \min\{ (\Phi/k_1)^{\varepsilon_1^{-1}}, \Phi/(k_1 \delta_{\Delta_1}^{(\varepsilon_1 - 1)}) \} \right\} . \tag{37}$$

At this moment, the formula (28) satisfies $\dot{V}(t) < 0$, and the proposed whole control system is stable.

Case 2: when the system states are in the close approximation phase, as shown in Fig. 4(b), this phase can be represented from $t_2 \to 0$. At this moment, $k_2 \text{Fal} \left(\sigma(t), \varepsilon_2, \delta_{\Delta_2} \right)$ plays a key role due to $0 < \varepsilon_2 < 1$. The convergence region follows (38) to ensure the stability of the controller system using a similar calculation process.

$$\Omega_2 : \left\{ |\sigma(t)| \, | \, |\sigma(t)| \leq \min\{ (\Phi/k_2)^{\varepsilon_2^{-1}}, \Phi/(k_2 \delta_{\Delta_2}^{(\varepsilon_2 - 1)}) \} \right\} . \tag{38}$$

From the calculation above, the whole controller makes the system states converge to the following convergence region in finite time:

$$|\sigma(t)| \leq \Psi = \min\{ \Omega_1, \Omega_2 \} . \quad \square \tag{39}$$

Remark 2. According to the formula (39), the steady-state error bound of the proposed FOSMC method is related to the Φ, and the parameters k_1, k_2 reduce the steady-state error bound. Different from the [42,43], the lump disturbance $\phi(t)$ is eliminated using the formula (21). Because the parameters of the two-power reaching law are obtained by trial-and-error method rather than the adaptive algorithm, the upper bound of the lump disturbance cannot be estimated. But it can reduce the "chattering phenomenon" and keep the system states on the sliding mode surface in a superior way.

Remark 3. It notes that the traditional reaching law of the SMC has the characteristics of "fast approach at long range, slow approach at close range". In this study, different from the existing reaching law, the proposed two-power reaching law (21) can make the states of the system reach the sliding mode surface at the faster speed and improve the robustness and convergence rate of the SMC. In generally, the system states entering the sliding surface at a faster speed will cause serious chattering phenomenon. However, the FOSMS can slow down the chattering amplitude when the system states reach $\sigma(t) = 0$, it is shown as Fig. 3. Therefore, the proposed FOSMC method based on two-power reaching law not only speeds up the reaching rate but also reduces the chattering of the controller.

4. Experimental facility

4.1. Description of experimental setup

The experimental setup of the PNS system and its corresponding structure diagram are illustrated in Fig. 5. The modeling and control schemes are verified on a commercial PNS (MPT-2MRL050, Boshi Robotics), which is composed of a piezoelectric actuator, a displacement sensor, and a mechanical structure. The system is built on a vibration reduction platform (J02-1809, Sunnylink), which avoids the negative influences of external disturbances. A host computer, equipped with 16-bit A/D and D/A converters (PCI-1710, Advantech), implements the proposed controller. An analog control input signal, which is produced by the DACs and subsequently amplified 15 times via the driver amplifier of the integral positioning controller (PPC-2CR0150, Boshi Robotics), is delivered to drive the PNS. The output displacement is measured in real-time by a built-in strain gauge sensor of the integral positioning controller, the actual output displacement value is converted into voltage signal by the ADCs, and it is used as the input of the proposed controller. Then, the control action of the proposed controller is obtained through calculation with the desired trajectory and the actual output displacement. Moreover, the proposed control strategies are carried out by Matlab/Simulink software (which is installed on the host computer and runs on Windows 10 and an Intel Core i7-1195G7 CPU) with the toolbox of the real-time windows target. The sampling time of the following experiments is set as 0.0001 s.

4.2. Identification of Duhem model

As mentioned above in the Duhem model, several parameters (i.e., a_0, a_1, a_2, f_i, g_i, and α) are unknown, and they must be estimated using the optimization algorithm. For ease of identification of the parameters of the Duhem model, the formula (7) without the lump disturbance ϕ is discretized and rewritten as:

$$\begin{cases} x(k) - x(k-1) = a_0 x(k) + a_1 u(k) + a_2 \hat{h}(u(k)) \\ \varphi(k) = \alpha |\tau(k)| \left[\sum_{i=0}^{p} f_i u^i(k-1) - \hat{h}(u(k-1)) \right] \\ \qquad + \tau(k) \sum_{j=0}^{q} g_j u^j(k-1) , \end{cases} \tag{40}$$
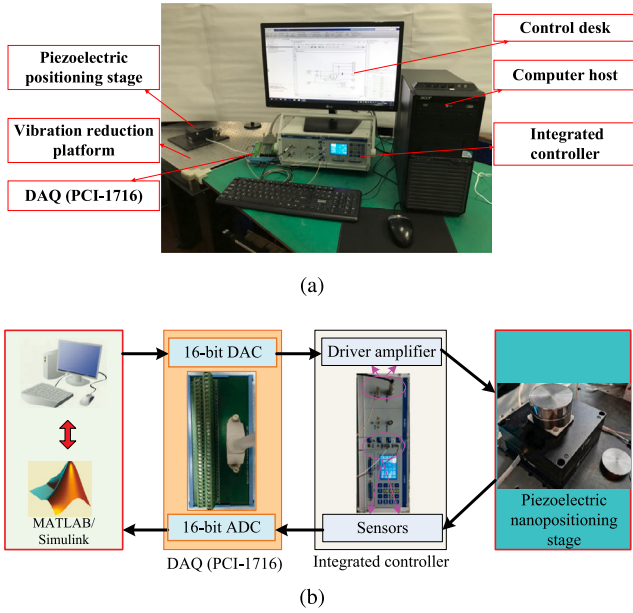
(a)

(b)

Fig. 5. Experimental setup. (a) picture of experimental platform, (b) structure diagram of experimental stage.
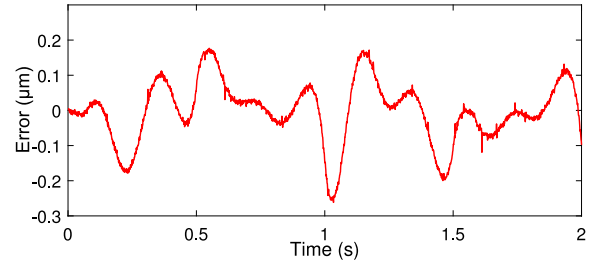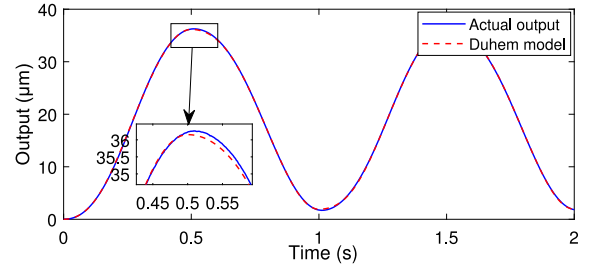

(a)

(b)

Fig. 6. Real output of the PNS and output of the Duhem model under sinusoidal inputs. (a) model curves, (b) model error.

Table 1
Parameters of three different controllers.

Controller	Parameters	Value
PID	k_p	0.5030
	k_i	1.1358
	k_d	0.0015
SMC	λ	2500
	η	0.225
FOSMC	λ	2000
	r	0.6
	$\varepsilon_1/\varepsilon_2$	2.1/0.9
	$\delta_{\Delta_1}/\delta_{\Delta_2}$	0.1/0.01
	k_1/k_2	400/300

where $\varphi(k) = \hat{h}(u(k)) - \hat{h}(u(k-1))$, $\tau(k) = u(k) - u(k-1)$, $p = 3$, $q = 2$, k represents the time state. In this study, to quantify the performance of the modeling and controller, we define the maximum (MAX), mean absolute (MA), and root-mean-square (RMS) error as follows:

$$\text{RMS} = \sqrt{\sum_{k=1}^{\eth} \frac{e^2(k)}{\eth}}, \tag{41}$$

$$\text{MAX} = \text{maximum} \, |e(k)|, \tag{42}$$

$$\text{MA} = \frac{\sum_{k=1}^{\eth} |e(k)|}{\eth}, \tag{43}$$

where $\eth$ is the number of datasets.

Then, we employ the interior point method in the MATLAB toolbox to obtain exact model parameters. The identified results of the Duhem model are shown in Fig. 6, and it is obvious that the Duhem model accurately captures the output of the actual PNS. The RMS error and MAX error of the identified Duhem model are 0.0761 μm and 0.69%, respectively.

5. Experimental study and discussion

The performance of the proposed FOSMC method is evaluated by a series of experiments. For comparison purposes, the PID and SMC methods are likewise implemented as following formulae (44) and (45). The parameters of these three controllers are obtained using the trial-and-error method. In this process, with the increase of the parameter λ, the tracking error will decrease, but too large λ will also produce system shocks; in addition, the fractional order r should be balanced with the parameters λ. The parameters k_1, k_2, η are selected based on the lump disturbance. For the parameters ε_1 and ε_1, we design that $\varepsilon_1 = 1.00001$ and $\varepsilon_2 = 0.99999$. Then, while keeping the ε_2 unchanged, increase the value of ε_1 until the FOSMC system produces a slight chattering. At this point, reduce the value of ε_2 to mitigate system chattering. According to the above rules, the parameters of these control methods are given in Table 1.

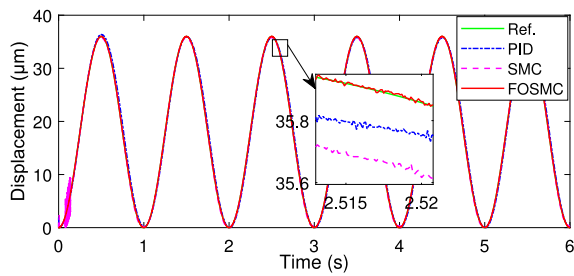$$u_{\text{pid}}(t) = k_p e(t) + k_i \int e(t)dt + k_d \dot{e}(t), \tag{44}$$

where k_p, k_i, and k_d represent the proportional, integral, and differential coefficients, respectively.

$$u_{\text{smc}}(t) = \frac{1}{a_1}[\dot{x}_d(t) - a_0 x(t) - a_2 \hbar(t) + \lambda e(t)] + \eta \text{sgn}(\sigma(t)). \tag{45}$$
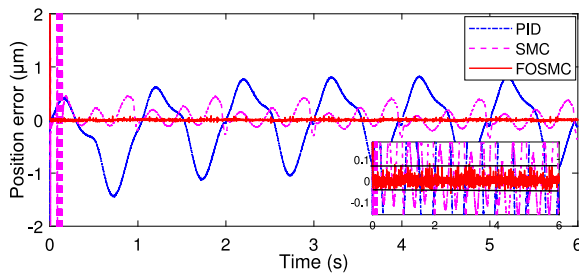
where η is the switching gain, it is a constant.

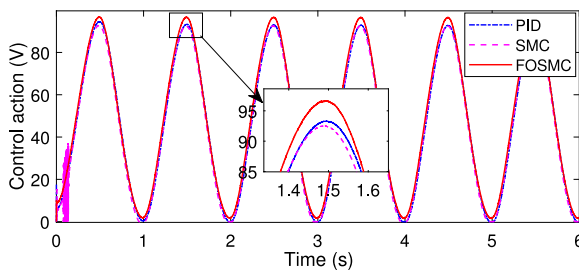### 5.1. Tracking experimental results of sinusoidal wave signal

To demonstrate the effectiveness of the proposed control scheme, the sinusoidal wave signal is used as the desired trajectory, which is denoted as $x_{\text{dsin}}(t) = 18\sin(2\pi f t - 0.5\pi) + 18$ ($f = 1, 50, 100$ Hz). For the purpose of comparison, we conducted tracking experiments with the other two types of controllers. Tracking results under different frequencies are presented in Figs. 7–9. It notes that the output displacement of the PNS is consistent with the desired trajectory, and the hysteresis effect and the lump disturbance are eliminated using the proposed controllers. The proposed FOSMC method was found to have the lowest positioning error, while the PID controller generates the maximum tracking error under different frequencies. When the frequency of the reference signal is 100 Hz, the RMS tracking errors of the PID, SMC, and FOSMC methods are 1.1520, 0.7766, and 0.4704 μm, respectively. Evidently, the tracking performance of the proposed FOSMC method is improved by 59.17% and 39.42% compared with the PID and SMC

Fig. 7. Sinusoidal trajectory tracking results of (a) tracking curves, (b) error curve, and (c) control action with 1 Hz signal rate with proposed controller.

Fig. 8. Sinusoidal trajectory tracking results of (a) tracking curves, (b) error curve, and (c) control action with 50 Hz signal rate with proposed controller.

Table 2
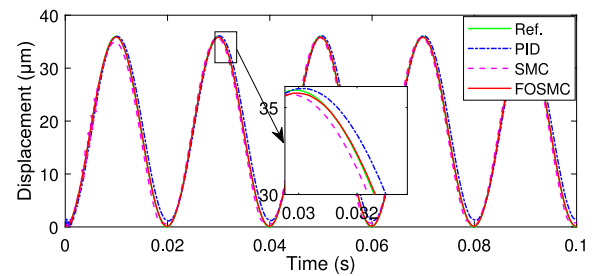Tracking results of three different controllers under sinusoidal wave signal.

Frequency (Hz)	RMS/MAX of PID (μm/%)	RMS/MAX of SMC (μm/%)	RMS/MAX of FOSMC (μm/%)
$f = 1$	0.4772/2.64	0.1503/1.07	0.0064/0.19
$f = 50$	0.9100/4.46	0.7133/3.34	0.1409/0.76
$f = 100$	1.1520/5.81	0.7766/5.04	0.4704/2.48

Table 3
Comparison between FOSMC method and existing controller.

Method	Frequency (Hz)	MAX (%)	MAX of FOSMC (%)	Improved (%)
Controller in [5]	$f = 1$	1.20	0.19	84.17
Controller in [7]	$f = 15$	0.98	0.35	64.29
Controller in [19]	$f = 50$	2.11	0.76	63.98
Controller in [23]	$f = 1$ and 5	0.94	0.18	80.85

method, respectively. The experimental data obtained with the elaborated controller are given in Table 2 and Fig. 10, where the trajectory tracking of the PNS is obtained with a great level of precision.
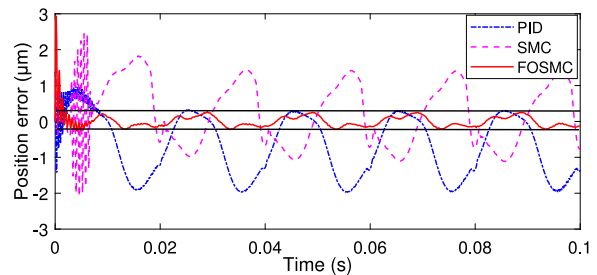
The control actions of different controllers are shown in Figs. 7(c)–9(c). When the frequency is 100 Hz, the control action of the SMC method produces some chattering, and the proposed FOSMC method has the smooth control actions from the magnified portion of Fig. 9(c). Hence, the chattering problem of the traditional SMC method is effectively resolved. The comparison results between the proposed FOSMC method and the ones in the literature are given in Table 3. The MAX tracking errors of the proposed FOSMC method are improved by more than 60% in comparison with existing control strategies.

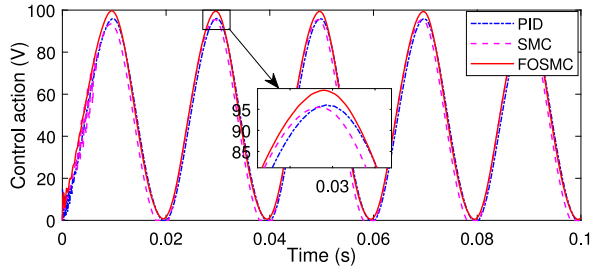*5.2. Tracking experimental results of complex triangular wave*

To further verify the control performance of FOSMC method, a complex triangular wave is employed as the desired reference trajectory.

Fig. 11 depicts the experiment results by using the different controller. As shown in Fig. 11, the FOSMC shows the prominent control effect for tracking complex triangular wave trajectory. The RMS errors of SMC and FOSMC methods are 0.0331 and 0.0109 μm, respectively. It is obvious that the tracking precision is greatly improved by FOSMC method. In addition, Fig. 11(c) shows that the sliding mode surface is constrained and the FOSMC drives the sliding mode surface to the range of ±0.4775 μm. However, the SMC drives the sliding mode surface to the range of ±0.8446 μm. In comparison with SMC, the proposed FOSMC method mitigates the sliding mode surface boundary by 43.46%.

5.3. Tracking experimental results with some different loads

To test the robustness of the proposed FOSMC approach, we carried out tracking control experiments by the PNS with different loads. In this experiment, the external loads are applied by five different weights.
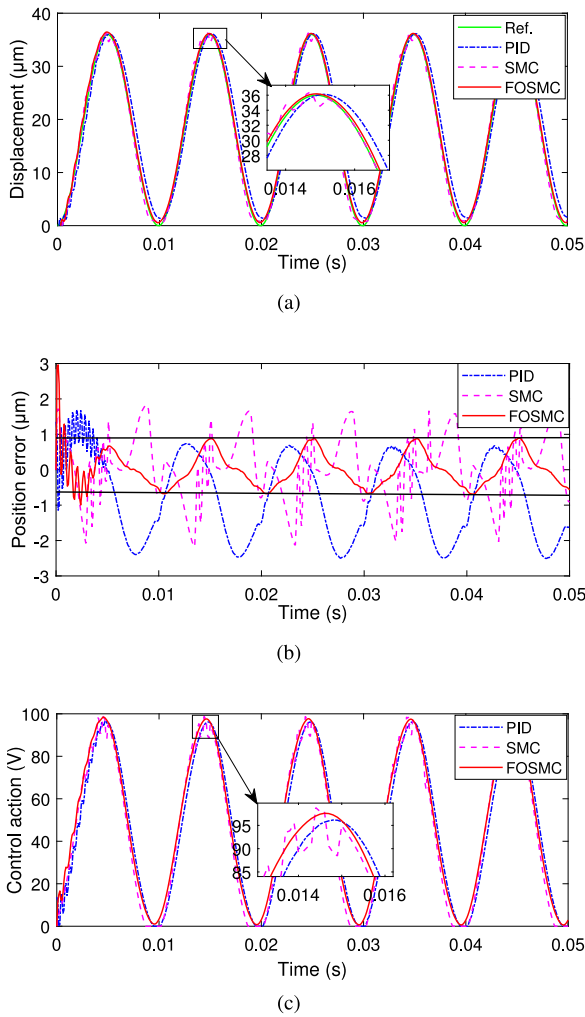
Fig. 9. Sinusoidal trajectory tracking results of (a) tracking curves, (b) error curve, and (c) control action with 100 Hz signal rate with proposed controller.
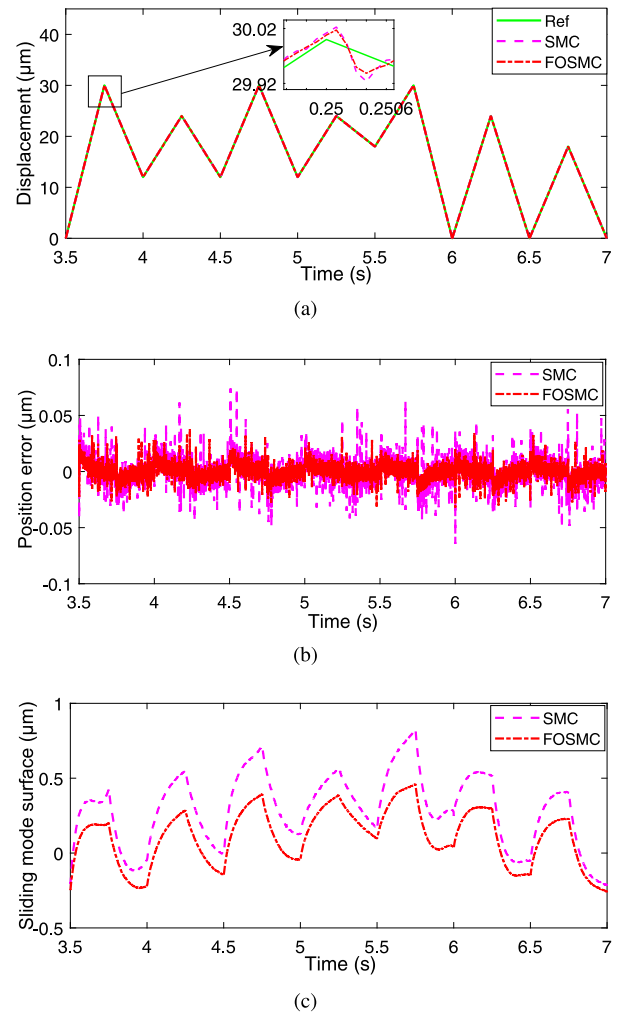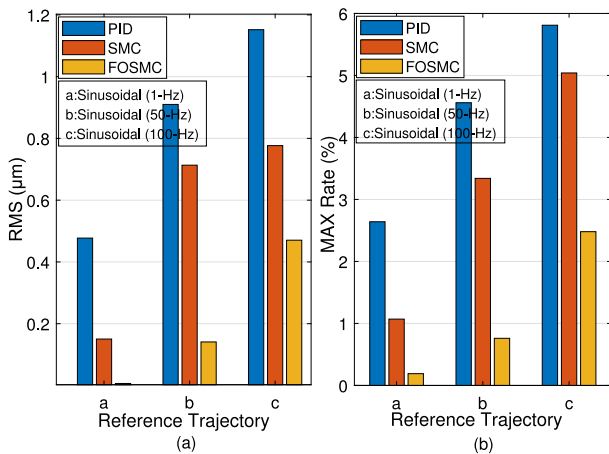

Fig. 10. Comparative tracking results of PID, SMC, and proposed FOSMC method. (a) RMS errors, (b) MAX rate.

With the reference signal as a 1 Hz sinusoidal wave signal, we mounted loads of 0, 100, 200, 300, 400, and 500 g onto the PNS to conduct the tracking experiments by the proposed FOSMC method. The MA errors and RMS tracking errors with different loads of the proposed control

Fig. 11. Complex triangular wave trajectory tracking results of (a) tracking curves, (b) error curves, and (c) sliding mode surface.

approach barely change. The comparative experimental results are shown in Fig. 12, where the horizontal axis and vertical axis are the supporting weights and evaluation index. The supporting weights include 0, 100, 200, 300, 400, and 500 g weights. The evaluation index includes MA and RMS. From Fig. 12, when the frequency of the reference trajectory signal is 100 Hz, the fluctuation range of the MA and RMS errors, based on the FOSMC method, is from ± 0.0041 μm and ± 0.0059 μm. Thus, experimental results show that the developed FOSMC method is robust against the external load disturbance.

6. Conclusion and future prospects

A FOSMC scheme, based on a two-power reaching law, was developed in this study for application in PNS. The convergence and stability of the proposed controller are analyzed and verified by theoretical calculations. In contrast to the comment sliding mode surface, the FOSMS decays slower than that with the integer order, which improves the performance of the FOSMC method. The new two-power reaching law improves the robustness and convergence rate of the proposed controllers. The performance of the proposed FOSMC scheme has been validated by comparative experiments. Results show that the FOSMC method outperforms the PID and SMC methods. Moreover, load experiments demonstrate high robustness of the FOSMC method. From comparative experimental results, the percentage improvement in RMS
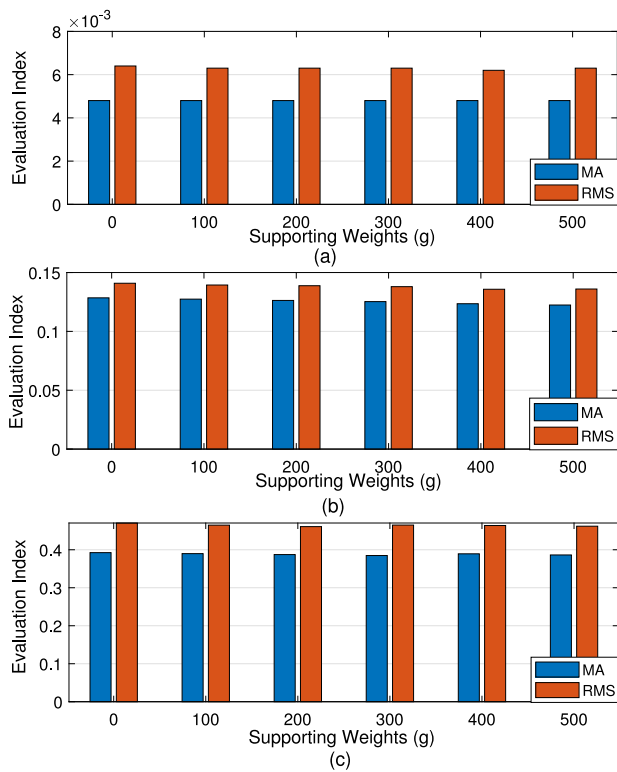
Fig. 12. Tracking experimental results of proposed controller with different loads. (a) 1 Hz, (b) 50 Hz, (c) 100 Hz.

error from SMC to FOSMC is 80.25% when the reference signal is sinusoidal trajectory with 50 Hz.

However, the parameters of the proposed controller are obtained by trial and error, which makes the design of controller parameters difficult. In the future, we will focus on the parameter tuning method of the FOSMC strategy and reduce this difficulty in obtaining controller parameters. In addition, the proposed FOSMC method is ultimately bounded stability. The appropriate adaptive law will be designed to estimate the upper bound of the lump disturbance and reduce the system stabilization error bounds.

CRediT authorship contribution statement

Rui Xu: Conceptualization, Methodology, Validation, Software, Writing – original draft. **Zhongshi Wang:** Formal analysis. **Miaolei Zhou:** Data curation, Editing. **Dapeng Tian:** Supervision, Project administration.

Declaration of competing interest

No potential conflict of interest was reported by the authors.

Data availability

Data will be made available on request

References

[1] H. Pota, I. Petersen, M. Rana, Creep, hysteresis, and cross-coupling reduction in the high-precision positioning of the piezoelectric scanner stage of an atomic force microscope, IEEE Trans. Nanotechnol. 12 (6) (2013) 1125–1134.

[2] K. Leang, S. Devasia, Feedback-linearized inverse feedforward for creep, hysteresis, and vibration compensation in AFM piezoactuators, IEEE Trans. Control Syst. Technol. 15 (5) (2007) 927–935.

[3] H. Amini, B. Farzaneh, F. Azimifar, et al., Sensor-less force-reflecting macro–micro telemanipulation systems by piezoelectric actuators, ISA Trans. 64 (2016) 293–302.

[4] M. Muraoka, S. Sanada, Displacement amplifier for piezoelectric actuator based on honeycomb link mechanism, Sensors Actuators A 157 (1) (2010) 84–90.

[5] B. Ding, Y. Li, Hysteresis compensation and sliding mode control with perturbation estimation for piezoelectric actuators, Micromachines 9 (5) (2018) 241.

[6] R. Xu, W. Pan, Z. Wang, et al., High-precision tracking control of a piezoelectric micro-nano platform using sliding mode control with the fractional-order operator, Int. J. Precis. Eng. Manuf. 21 (12) (2020) 2277–2286.

[7] M. Nguyen, X. Chen, F. Yang, Discrete-time quasi-sliding-mode control with prescribed performance function and its application to piezo-actuated positioning systems, IEEE Trans. Ind. Electron. 65 (1) (2018) 942–950.

[8] M. Rakotondrabe, Bouc-wen modeling and inverse multiplicative structure to compensate hysteresis nonlinearity in piezoelectric actuators, IEEE Trans. Autom. Sci. Eng. 8 (2) (2011) 428–431.

[9] R. Li, Y. Feng, Z. Hu, Dynamic surface control of shape memory alloy actuating systems with inverse duhem hysteresis compensation, in: Proc. of 2018 IEEE International Conference on Mechatronics and Automation, 2018, pp. 1305–1310.

[10] M.A. Janaideh, S. Rakheja, C. Su, An analytical generalized Prandtl–Ishlinskii model inversion for hysteresis compensation in micropositioning control, IEEE/ASME Trans. Mechatronics 16 (4) (2011) 734–744.

[11] Z. Li, Y. Xu, X. Yang, J. Feng, W. Fang, Generalized inverse multiplicative structure for differential equation based hysteresis models, IEEE Trans. Ind. Electron. 68 (5) (2021) 4182–4189.

[12] R. Xu, D. Tian, M. Zhou, A rate-dependent KP modeling and direct compensation control technique for hysteresis in piezo-nanopositioning stages, J. Intell. Mater. Syst. Struct. 33 (5) (2022) 629–640.

[13] J. Lin, H. Chiang, C. Lin, Tuning PID control parameters for micro-piezo-stage by using grey relational analysis, Expert Syst. Appl. 38 (11) (2011) 13924–13932.

[14] H. Ghafarirad, S.M. Rezaei, A. Abdullah, M. Zareinejad, M. Saadat, Observer-based sliding mode control with adaptive perturbation estimation for micropositioning actuators, Precis. Eng. 35 (2) (2011) 271–281.

[15] Y. Jian, D. Huang, J. Liu, D. Min, High-precision tracking of piezoelectric actuator using iterative learning control and direct inverse compensation of hysteresis, IEEE Trans. Ind. Electron. 66 (1) (2019) 368–377.

[16] M. Edardar, X. Tan, H. Khalil, Design and analysis of sliding mode controller under approximate hysteresis compensation, IEEE Trans. Control Syst. Technol. 23 (2) (2015) 598–608.

[17] Y. Al-Nadawi, X. Tan, H. Khalil, Inversion-free hysteresis compensation via adaptive conditional servomechanism with application to nanopositioning control, IEEE Trans. Control Syst. Technol. 29 (5) (2020) 1922–1935.

[18] J. Lee, M. Jin, N. Kashiri, et al., Inversion-free force tracking control of piezoelectric actuators using fast finite-time integral terminal sliding-mode, Mechatron 57 (2019) 39–50.

[19] R. Xu, M. Zhou, A self-adaption compensation control for hysteresis nonlinearity in piezo-actuated stages based on Pi-sigma fuzzy neural network, Smart Mater. Struct. 27 (4) (2018) 045002.

[20] W. Liu, L. Cheng, Z. Hou, J. Yu, M. Tan, An inversion-free predictive controller for piezoelectric actuators based on a dynamic linearized neural network model, IEEE/ASME Trans. Mechatronics 21 (1) (2016) 214–226.

[21] R. Xu, D. Tian, Z. Wang, Adaptive tracking control for the piezoelectric actuated stage using the Krasnosel'skii-Pokrovskii operator, Micromachines 11 (5) (2020) 537.

[22] Q. Xu, Digital integral terminal sliding mode predictive control of piezoelectric-driven motion system, IEEE Trans. Ind. Electron. 63 (6) (2016) 3976–3984.

[23] R. Xu, X. Zhang, H. Guo, M. Zhou, Sliding mode tracking control with perturbation estimation for hysteresis nonlinearity of piezo-actuated stages, IEEE Access 6 (2018) 30617–30629.

[24] A. Levant, M. Livne, Weighted homogeneity and robustness of sliding mode control, Automatica 72 (2016) 186–193.

[25] H. Ren, X. Wang, J. Fan, et al., Fractional order sliding mode control of a pneumatic position servo system, J. Franklin Inst. 356 (12) (2019) 6160–6174.

[26] J. Wang, C. Shao, Y. Chen, Fractional order sliding mode control via disturbance observer for a class of fractional order systems with mismatched disturbance, Mechatron 53 (2018) 8–19.

[27] S. Chen, H. Chiang, T. Liu, et al., Precision motion control of permanent magnet linear synchronous motors using adaptive fuzzy fractional-order sliding-mode control, IEEE/ASME Trans Mechatronics 24 (2) (2019) 741–752.

[28] B. Zhang, Y. Pi, Y. Luo, Fractional order sliding-mode control based on parameters auto-tuning for velocity control of permanent magnet synchronous motor, ISA Trans. 51 (5) (2012) 649–656.

[29] A. Calderón, B. Vinagre, V. Feliu, Fractional order control strategies for power electronic buck converters, Signal Process. 86 (10) (2006) 2803–2819.

[30] Q. Xu, Precision motion control of piezoelectric nanopositioning stage with chattering-free adaptive sliding mode control, IEEE Trans. Autom. Sci. Eng. 14 (1) (2016) 238–248.

[31] J. Slotine, W. Li, et al., Applied Nonlinear Control, Prentice hall, Englewood Cliffs, NJ, 1991.

[32] J. Wang, Q. Zong, R. Su, B. Tian, Continuous high order sliding mode controller design for a flexible air-breathing hypersonic vehicle, ISA Trans. 53 (3) (2014) 690–698.

[33] D. Haghighi, S. Mobayen, Design of an adaptive super-twisting decoupled terminal sliding mode control scheme for a class of fourth-order systems, ISA Trans. 75 (2018) 216–225.

[34] S. Oucheriah, L. Guo, PWM-based adaptive sliding-mode control for boost DC-DC converters, IEEE Trans. Ind. Electron. 60 (8) (2013) 3291–3294.

[35] H. Shieh, P. Huang, Precise tracking of a piezoelectric positioning stage via a filtering-type sliding-surface control with chattering alleviation, IET Control Theory Appl. 1 (3) (2007) 586–594.

[36] R. Keyser, C. Muresan, C. Ionescu, An efficient algorithm for low-order direct discrete-time implementation of fractional order transfer functions, ISA Trans. 74 (2018) 229–238.

[37] Q. Song, X. Yang, C. Li, et al., Stability analysis of nonlinear fractional-order systems with variable-time impulses, J. Franklin Inst. 354 (7) (2017) 2959–2978.

[38] T. Nonnenmacher, R. Metzler, On the Riemann–Liouville fractional calculus and some recent applications, Fractals 3 (3) (1995) 557–566.

[39] A. Oustaloup, F. Levron, B. Mathieu, F.M. Nanot, Frequency-band complex noninteger differentiator: characterization and synthesis, IEEE Trans. Circuits Syst. 47 (1) (2000) 25–39.

[40] E. E. Ahmed, A. El-Sayed, H. El-Saka, Equilibrium points, stability and numerical solutions of fractional-order predator–prey and rabies models, J. Math. Anal. Appl. 325 (1) (2007) 542–553.

[41] A. Polyakov, L. Fridman, Stability notions and Lyapunov functions for sliding mode control systems, J. Franklin Inst. 351 (4) (2014) 1831–1865.

[42] L. Qiao, W. Zhang, Trajectory tracking control of AUVs via adaptive fast nonsingular integral terminal sliding mode control, IEEE Trans. Ind. Inform. 16 (2) (2019) 1248–1258.

[43] L. Qiao, W. Zhang, Double-loop integral terminal sliding mode tracking control for UUVs with adaptive dynamic compensation of uncertainties and disturbances, IEEE J. Oceanic Eng. 44 (1) (2018) 29–53.

Rui Xu received the Ph.D. degree in control theory and control engineering with the Department of Control Science and Engineering, Jilin University, Changchun, China, in 2019. From Sep. 2018 to Sep. 2019, he was an exchange PhD student with the Department of Electrical and Computer Engineering, Michigan State University, East Lansing, USA. Since 2020, he has been with the Key Laboratory of AOIM, CIOMP, CAS, Changchun, China, where he is currently an Associate Researcher. His current research interests include micro-nano drive control, motion control theory and optical imaging.

Zhongshi Wang received the M.Eng. degree in control theory and control engineering with the College of Automation, Haerbin Engineering University, China, in 2014. He received the Ph.D. degree in mechatronic engineering from University of Chinese Academy of Sciences in 2021. He is currently an assistant researcher in the Key Laboratory of Airborne Optical Imaging and Measurement (AOIM), Changchun Institute of Optics, Fine Mechanics and Physics (CIOMP), Chinese Academy of Sciences (CAS), Changchun, China. His research interests include micro-nano control and motion control.

Miaolei Zhou received the B.S. and M.S. degrees in industrial electric automation from the Jilin Institute of Technology, Changchun, China, in 1997 and 2000, respectively, and the Ph.D. degree in control theory and control engineering from Jilin University, Changchun, in 2004. From October 2006 to September 2008, he was a Postdoctoral Researcher with Tokyo University, Tokyo, Japan. In 2000, he joined the Department of Control Science and Engineering, Jilin University, where he became an Associate Professor, in 2009, and a Professor, in 2014. He has supervised more than 20 research projects and authored more than 90 research papers. His research interests include modeling and control for micro/nanodevices and systems, nonlinear control theory, and navigation and control of robot. Dr. Zhou is a Vice Chairman of the Jilin Province Association of Automation, and a Member of the Technical Committee on Data Driven Control, Learning and Optimization, and Chinese Association of Automation.

Dapeng Tian received the B.E. degree from Beijing Institute of Technology, Beijing, China, in 2007. He was then directly recommended to study at Beihang University, Beijing, where he received the Ph.D. degree in 2012. From 2009 to 2011, he was a Co-researcher with the Advanced Research Center, Keio University, Yokohama, Japan. Since 2012, he has been with the Key Laboratory of AOIM, CIOMP, CAS, Changchun, China, where he is currently a Full Professor. His current research interests include motion control theory and engineering, optical imaging, and bilateral control.